Spin state-tailored tetrahedral and octahedral cobalt centers on millimetric Co-Al oxide catalysts as dual sites for synergistic peroxymonosulfate activation

Jia-Cheng E. Yang [a,b,1], Min-Ping Zhu [a,b,1], Daqin Guan [c], Baoling Yuan [d], Darren Delai Sun [e], Chenghua Sun [f], Ming-Lai Fu [a,g,*]

[a] *Key Laboratory of Urban Pollutant Conversion, Institute of Urban Environment (IUE), Chinese Academy of Sciences (CAS), No. 1799, Jimei Avenue, Xiamen 361021, China*
[b] *University of Chinese Academy of Sciences (UCAS), No. 19(A), Yuquan Road, Shijingshan District, Beijing 100049, China*
[c] *Department of Building and Real Estate, The Hong Kong Polytechnic University, Hung Hom, Kowloon 999077, Hong Kong, China*
[d] *Key Laboratory of Songliao Aquatic Environment, Ministry of Education, Jilin Jianzhu University, Changchun 130118, China*
[e] *School of Civil and Environmental Engineering, Nanyang Technological University, 639798, Singapore*
[f] *Faculty of Science, Engineering & Technology, Swinburne University of Technology, Victoria 3122, Australia*
[g] *Xiamen Key Laboratory of Municipal and Industrial Solid Waste Utilization and Pollution Control, College of Civil Engineering, Huaqiao University, Xiamen 361020, China*

A B S T R A C T

Rationally developing millimetric metal catalysts with tailored electron function is crucial for water decontamination, but challenges remain due to insufficient understanding on their electronic structure engineering and the underlying mechanism. Here, through constructing bonded Co-O-Al unit sites on the millimetric γ-Al$_2$O$_3$ spheres, we report a feasible and scalable strategy of modulating the 3d electron configurations and spin states of supported tetrahedral and octahedral cobalt cations just by adjusting the radius of support curvature. The tetrahedral and octahedral cobalt centers with tailored electron spin states showed a synergism in peroxymonosulfate activation to generate SO$_4^{\bullet-}$ and reactive oxygen (O*), in which the latter was converted into ^{1}O$_2$ and O$_2^{\bullet-}$. The electronic structure-oriented spin catalysis affected the formation of reactive species and the pathway of pollutant degradation. This work will stimulate the design and mass production of macroscopic spin catalysts with superior activity, reusability and stability for catalytic water purification.

1. Introduction

The frequent occurrence of emerging organic contaminants (EOCs) in the municipal sewages and their deleterious impacts on the ecological and human health call for an urgent need of developing effective and sustainable solutions to eliminate EOCs from polluted water [1–6]. Among various decontamination solutions, heterogenous advanced oxidation processes (AOPs) can serve as an attractive option [6,7]. Specially, nonprecious metal catalysts-oriented peroxymonosulfate (PMS) oxidation techniques have been considered as promising solutions to degrade a diversity of refractory EOCs due to the formation of highly reactive hydroxyl radical ($^{\bullet}$OH, 1.8 – 2.7 V$_{NHE}$), sulfate radical

(SO$_4^{\bullet-}$, 2.5 – 3.1 V$_{NHE}$) as well as [6–8]. The electron transfer between PMS and the surface metal sites of catalysts is generally considered as the primary force to generate such reactive species [9,10]. Therefore, various strategies such as manipulating the synergism of metal components [11,12], enlarging the metal-O covalency in a special coordination configuration [13], creating structure defects on the catalyst surface [14], and tailoring the metal-support interactions [15] have been intensively explore to enhance the electron transfer of metal surface catalysis for PMS activation. All these findings demonstrate that modulating the electronic structure of nonprecious metal catalysts is an effective way of improving their electron transfer-mediated surface catalysis reactions.

---

* Corresponding author at: Key Laboratory of Urban Pollutant Conversion, Institute of Urban Environment (IUE), Chinese Academy of Sciences (CAS), No. 1799, Jimei Avenue, Xiamen 361021, China.

E-mail addresses: mlfu@iue.ac.cn, mlfu@hqu.edu.cn (M.-L. Fu).
[1] These authors contributed equally to this work.

As an emerging electronic structure engineering, modulating the electron spin states of transition metals is receiving the attention of materials chemists due to its unique promotion in electron transfer [16–20]. For example, the construction of N-coordinated high-spin (HS) Co^{2+} in Co-Fe Prussian blue analogues contributed to their excellent activity in PMS activation via elongating SO_4-OH bond length, strengthening adsorption and facilitating electron transfer over the activation process [16]. The introduction of Li ions into Co-based metal-organic frameworks can induce the formation of HS-Co^{2+} and thus enhance their catalytic activity in organic degradation [17]. The metal vacancies and coordination structures-regulated spin polarization has demonstrated an improved electron transfer for pollutant photo-degradation with Ti-based composite catalysts [18,19]. However, the metal electron spin state-related AOPs are still in a fledging period considering the following technical bottlenecks: (i) The existing procedures for the electron spin state modulation of catalysts are generally time- and energy-intensive and therefore, not conducive to their mass production [19]. (ii) The available catalysts are usually present as powders and inefficient for their recycling and reuse under concessive operation conditions for practical applications [18,20]. (iii) Moreover, the nano/micro-scaled powder catalysts are apt to aggregate and produce sludge, thus causing poor mass transfer, potential toxicity risks and secondary pollution for wastewater deep purification [8,9].

In this regard, constructing the active metal species on millimeter/centimeter-scale substrates as macroscopic catalysts appears to be a wise solution to overcome the above engineering bottlenecks [21–23]. More importantly, the key advantage of such practice lies in the flexibility of integrating these macroscopic catalysts into advanced reactors/devices — which can easily form a tandem purification system when combined with the existing wastewater treatment processes. Compared with foams/sponges [22,23], activated carbon pellets [24], and membranes [25,26], millimetric γ-Al_2O_3 spheres are preferentially used as the supports to develop macroscopic catalysts for the real water purification due to their high mechanical strength, low cost, changeable surface sites and easy recovery [27,28]. By virtue of the higher standard reduction potential of cobalt (Co^{3+}/Co^{2+}, $E^0 = 1.92$ V) than other transition metals [29], various cobalt-based macroscopic catalysts have been intensively studied for PMS activation [21,24,30–32]. Nevertheless, up to now, how to rationally and cost-effectively modulate the Co 3*d* electron spin states is quite challenging for the mass production of macroscopic catalysts. Moreover, the kinetic consequence of electron spin state modulation on PMS activation and the corresponding principle of governing the radical production are still lack of investigation.

Herein, we develop a scalable and feasible impregnation-calcination integrated process to precisely modulate the 3*d* electron spin states of tetrahedrally and octahedrally coordinated cobalt cations on the millimetric γ-Al_2O_3 spheres via constructing Co-O-Al bridge bonds and controlling the radius of support curvature (i.e., the inverse of the support radius). Then, we used UV–vis, X-ray photoelectron spectroscopy (XPS) and X-ray absorption spectra (XAS) at Co-*L* edges and O-*K* edges to systematically disentangle the changeable coordination configurations, elemental valence and electron spin states of cobalt centers induced by support curvature (i.e., the bottom of the support radius). Experimental and theoretical investigations indicate that the synergism of spin state-tailored tetrahedral and octahedral cobalt cations within millimetric Co-Al oxide catalysts controlled the PMS activation, thus resulting in $SO_4^{\bullet-}$ and $^1O_2$-dominated oxidation processes for the removal of EOCs. The developed millimetric spin catalysts are cheaper than commercial Co-based powder catalysts. This study will provide a simple and reliable method to tailor/engineer the electron spin state-oriented function within macroscopic metal catalysts for efficient water purification.

2. Experimental section

2.1. Materials

The millimetric γ-Al_2O_3 spheres with different diameter ranges (i.e., 1 – 2 mm, 3 – 5 mm, and 8 – 10 mm) were supplied by Henan Zhongbang Environmental Protection Technology Co., Ltd. (China). The details of other chemicals can be found in Text S1 and used without further treatments. Prior to catalyst preparation, the millimetric spheres were washed with abundant deionized water and dried at 105 °C.

2.2. Catalyst synthesis

The millimetric Co_2AlO_4 composite catalysts were prepared using an integrated process of impregnation and calcination. For simplicity, we denoted the catalysts from γ-Al_2O_3 spheres with a diameter range of 1 – 2 mm (high curvature), 3 – 5 mm (moderate curvature), and 8 – 10 mm (low curvature) as HCA, MCA and LCA, respectively. In detail, HCA samples were prepared as following steps: Firstly, the pretreated γ-Al_2O_3 spheres (60 g, 1 – 2 mm in diameter) were fully immersed into Solution A (240 mM of 2-methylimidazole in deionized water) for 30 min without stirring, followed by a washing step with deionized water for three times. Subsequently, the resultant spheres were placed into Solution B (30 mM of $Co(NO_3)_2 \cdot 6\ H_2O$ in deionized water) for another 30 min without stirring. After washing with deionized water, the samples were immediately transferred into the mixtures of Solution A and B without disturbance. After aging for 24 h, the pink samples were separated and washed with deionized water for several times, and dried at 105 °C overnight. Finally, the as-prepared samples were calcined under 550 °C for 3 h in static air with a heating rate of 2 °C/min. After cooling to room temperature naturally, the dark green products were obtained. Identical procedures were repeated to prepare MCA (or LCA) except replacing pretreated γ-Al_2O_3 spheres with a diameter range of 3 – 5 mm (or 8 – 10 mm).

2.3. Catalyst characterization

The high-angle annular dark-field scanning transmission electron microscopy (HAADF-STEM) images and energy dispersive spectrometer (EDS) mappings of catalysts were taken on an instrument of Thermo Fisher Scientific Spectra 300 S/TEM equipped with double spherical aberration corrector (operated at 300 kV). The Co *L*-edge X-ray absorption spectra (XAS) of catalysts were performed at the BL20A high-energy spherical grating monochromator beamline of the National Synchrotron Radiation Research Center (NSRRC) in Taiwan, and Co foil and CoO single crystal samples were measured simultaneously for the energy correction of Co-$L_{2,3}$ XAS spectra, respectively. The Co-$L_{2,3}$ XAS spectra were obtained using the total electron yield mode. To probe the change of both electronic spin state and valence state of cobalt, we simulated the Co-L_3 XAS spectra of catalysts via a method of superposing the references of cobalt oxides [33–35]. The Co *K*-edge X-ray absorption fine structure and near-edge structure (XAFS/XANES) spectra were collected at the 44 A beam line of NSRRC in Taiwan. The detailed fitting parameters of extended XAFS and Wavelet transform can be found in Text S2, while the testing information of X-ray diffraction (XRD), UV–vis spectra, Brunauer-Emmett-Teller (BET) surface area, transmission electron microscopy (TEM), X-ray photoelectron spectroscopy (XPS) and inductively coupled plasma optical emission spectroscopy (ICP-OES) can be found in Text S3.

2.4. Activity measurements

Batch experiments were performed in 100 mL conical flasks, which were loaded in an orbital shaker (300 rpm) at 25 ± 1 °C. In a typical test, 80 mL of carbamazepine (CBZ) (10 mg/L) and 20 g/L catalysts (i.e., HCA, MCA or LCA) were added into the flasks. Then, the catalytic

reactions were triggered by introducing 0.2 g/L PMS into the above system. At different intervals, 1 mL aqueous sample was withdrawn, immediately quenched with 0.25 mL ethanol, and filtered through a 0.22 μm hydrophilic membrane. Identical procedures were conducted using bisphenol A (BPA), butyl paraben (BPB), 2-chlorophenol (2-CP) and phenol as the target pollutants. Quenching experiments were also carried out using ethanol (EtOH), tert-butyl alcohol (TBA), histidine (HD) and benzoquinone (BQ) as scavengers, and the method for calculating the inhibition rates of different scavengers in CBZ removal can be found in Text S4. In order to evaluate the recyclability of catalysts, the HCA samples after reaction were separated after each test, washed with enough DI water, dried at 105 °C for 2 h, and then used in the next test. All the tests were performed in duplicate.

The residual concentrations of CBZ, BPA, BPB, 2-CP, and phenol were detected using a high-performance liquid chromatography (HPLC) system (Agilent 1260, USA). The detailed analysis methods are available in Table S1. The injection volume of all the samples for HPLC testing was set as 25 μL. The concentrations of leached Co ions in the aqueous systems were determined by an ICP-OES. The oxidation products of CBZ were detected by a HPLC/mass spectrometry (MS)/MS system (Thermo Scientific Q Exactive Ultimate 3000 UPLC, USA), and then their toxicities were assessed by adopting the Toxicity Estimation Software Tool (T.E.S.T. V4.1, developed by United States Environmental Protection Agency) according to a variety of quantitative structure activity relationship (QSAR) methodologies. Four kinds of toxicity indexes, including bioaccumulation factor (BAF), mutagenicity, *Daphnia magna* LC50 and *Oral rat* LD50, were predicted from the *Consensus* method. The detailed calculation on the normalized toxicity index can be found in Text S5.

2.5. Theoretical calculation

In order to reveal the catalytic activation mechanism of model catalysts, we have performed spin-polarized calculations based on the density functional theory (DFT) using the CASTEP (Cambridge sequential total energy package). More information can be available in Text S6.
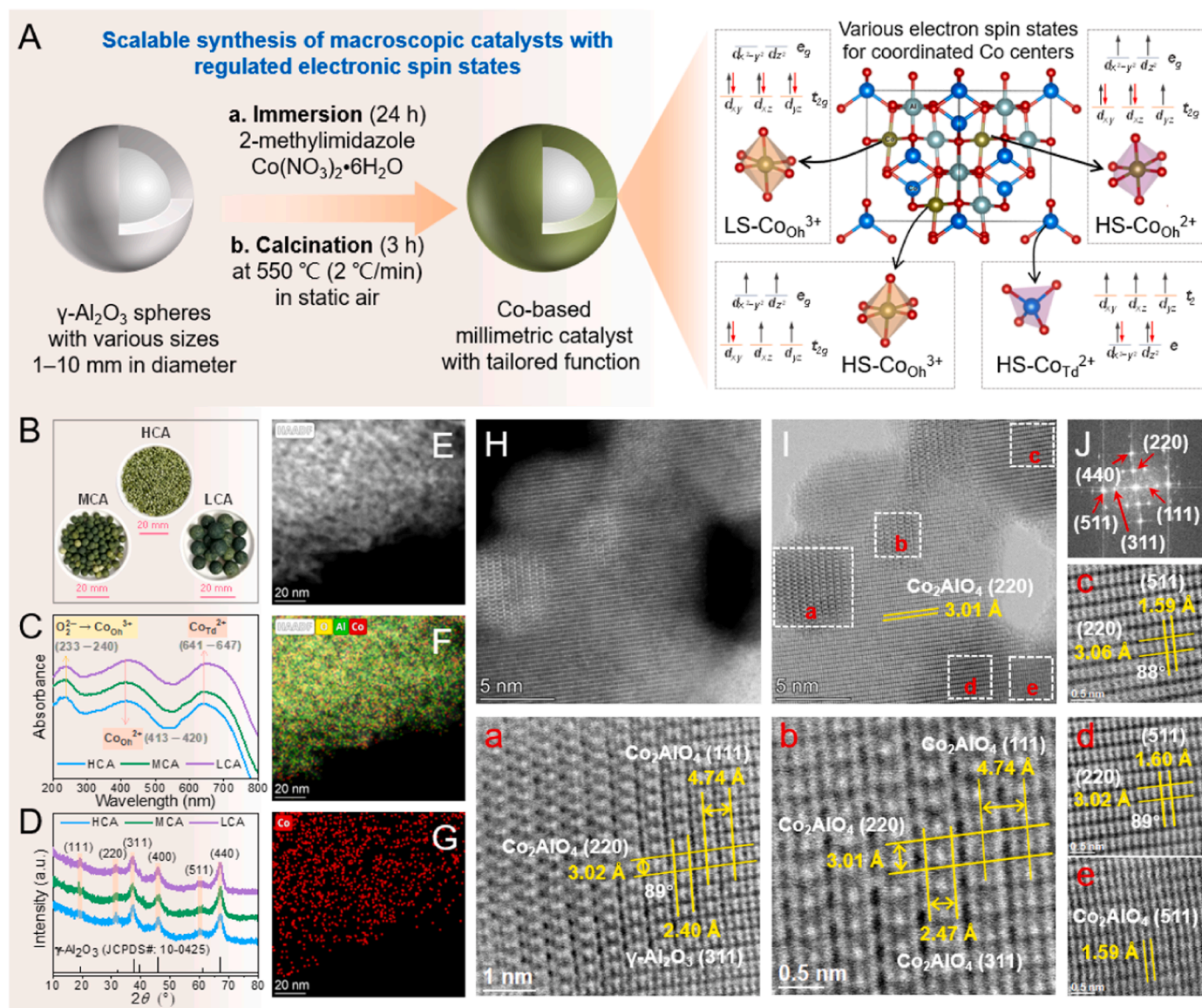
Fig. 1. Catalyst synthesis and characterization. (A) Schematic diagram on the scalable synthesis and electronic spin state modulation of millimetric Co$_2$AlO$_4$-based nanocomposite catalysts. (B) The optical images, (C) UV–vis spectra and (D) XRD patterns of HCA, MCA, and LCA. (E-D) The EDS mappings of HAADF-STEM for HCA and its typical HAADF-STEM images in dark field model (H) and transmission model (I). (J) The fast Fourier transform of HAADF-STEM image of (I) and (a-e) the enlarged images for the selected crystalline areas from (I).

3. Results and discussion

3.1. Structural characteristics of catalysts

The millimetric cobalt-based catalysts with tunable electronic structures were synthesized by a feasible room impregnation process coupling with calcination under air atmosphere (Fig. 1A). The resultant HCA, MCA and LCA are present in their dark green (Fig. 1B). As illustrated in Fig. 1C, the adsorption bands of UV–vis spectra of HCA, MCA and LCA at 233 – 240 nm indicate the ligand to metal charge transfer from O_2^{2-} to Co^{3+} in the octahedral sites [36], while the bands at 413 – 420 nm suggest the Co^{2+} in octahedral sites [37]. The bands at 641 – 647 nm evidence the presence of Co^{2+} in tetrahedral coordination [36, 38]. In all, all these signals suggest the characteristics of Co_2AlO_4 on γ-Al_2O_3 support. The catalysts appeared in their dark-green color are due to the light absorption at 233 – 240 nm and 413 – 420 nm. However, besides the XRD peaks of γ-Al_2O_3 support (JCPDS#: 10–0425) (Fig. 1D),

no signals of Co_2AlO_4 phase and other Co-related species were discerned for HCA, MCA and LCA samples. We think this is ascribed to the hyper-dispersion of cobalt elements and their relatively low loadings on γ-Al_2O_3 support (< 0.15 wt%, detected by ICP-OES). BET characterizations indicate that HCA, MCA and LCA are mesoporous catalysts, and their surface areas are 212.65, 200.68, and 191.38 m^2/g, respectively (Fig. S1 and Table S2).

The element distribution and crystallinity of typical cobalt-based nanocomposites (i.e., HCA) was characterized by aberration-corrected HAADF-STEM and high-resolution TEM. The EDS mappings of HAADF-STEM show the even distribution of Co elements throughout the support matrix (Fig. 1(E – G)), implying the uniform intercalation of Co atoms into γ-Al_2O_3 framework. The discontinuous selected-area electron diffraction of TEM shows coexisting diffraction spots and diffuse-ring, corresponding to the crystalline and amorphous domains of HCA, respectively (Fig. S2(A – B)). The bright areas appeared in the selected HAADF-STEM image (in dark field model) (Fig. 1H) suggest the
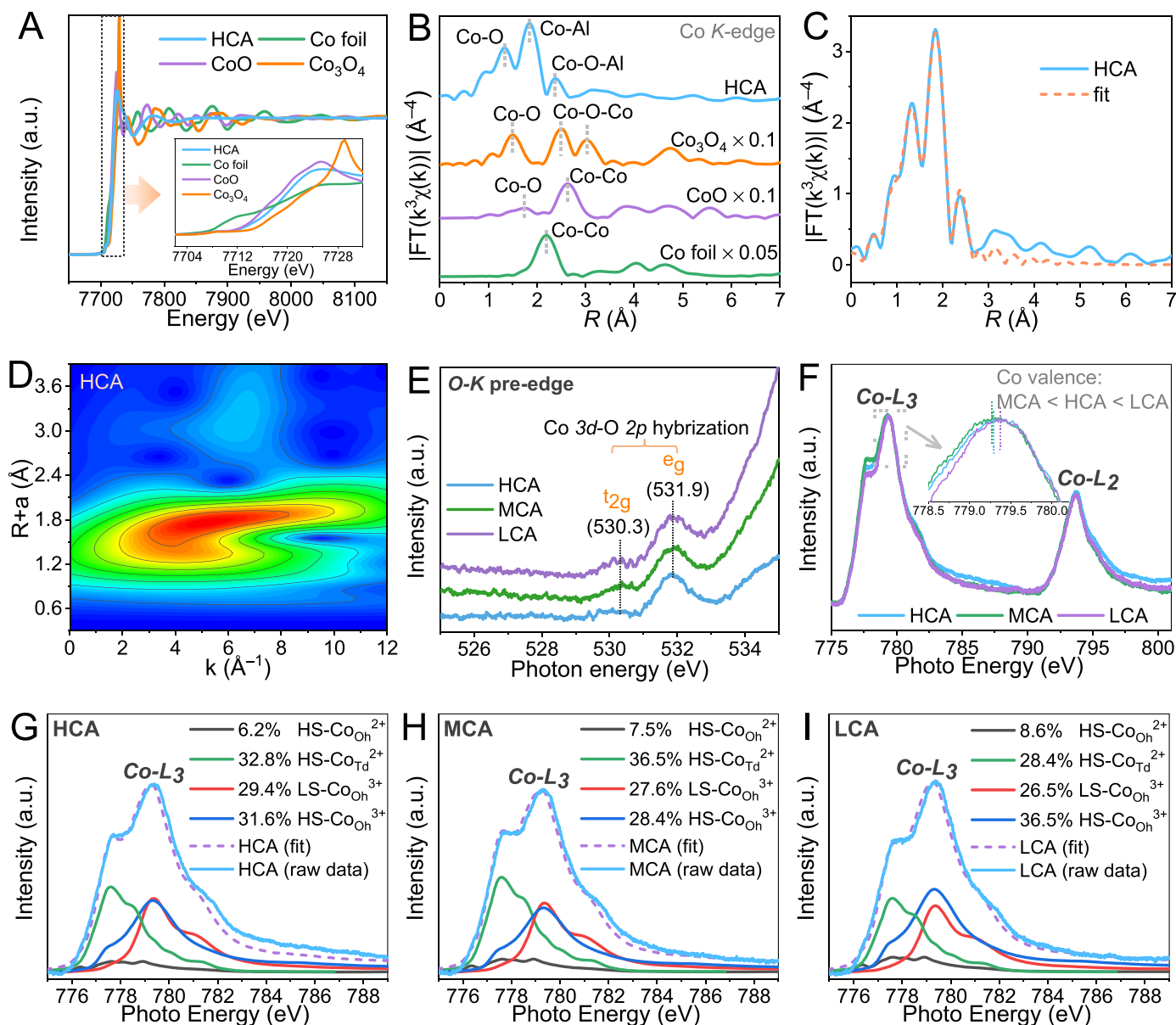
Fig. 2. **The coordination environment, elemental valence, and electronic configurations and spin states of cobalt centers within catalysts.** (A) The Co *K*-edge XANES spectra, (B) The k^3-weighted Fourier-transformed Co *K*-edge extended XAFS spectra, (C) the corresponding extended XAFS curve fitting at *R* space and (D) Wavelet transform for HCA. (E) The O *K*-edge XAS, and (F) the Co $L_{2,3}$-edge XAS for HCA, MCA and LCA, as well as the fitted Co L_3-edge XAS for HCA (G), MCA (H) and LCA (I).

successful intercalation of Co atoms into the lattices of support. The same HAADF-STEM image in transmission model and its fast Fourier transform (Fig. 1(I – J)) clearly verify the nature of heterogeneous lattices of catalyst. As seen in the enlarged areas (a – e) of Fig. 1I, the interplanar spacings of 4.74 Å, 3.01 – 3.06 Å, 2.47 Å, 1.59 Å and 1.47 Å are attributed to the (111), (220), (311), (511) and (440) planes of Co_2AlO_4 (PDF#38–0814), while the spacing of 2.4 Å is due to the (311) plane of γ-Al_2O_3 (PDF#10–0425). The dominant (220) facet is nearly perpendicular to the (511) facet and (111) facet. In all, the investigations of HAADF-STEM and XRD imply that the immobilized cobalt species are ultra-dispersed and the sizes of Co-based active crystalline domains are in the quantum scale.

The possible bonding/coordination between Co atoms and Al/O elements in HCA was determined by XAS. As shown in Fig. 2A, the normalized Co K-edge XANES spectrum of HCA is located between CoO and Co_3O_4, suggesting that the average valence state of Co within HCA is located at 2 – 2.7. Fig. 1B depicts the Fourier transformed k^3-weighted extended XAFS spectrum of HCA. The first shell peak at 1.86 Å is representative of Co-O bond. Two separate peaks at ∼ 2.33 Å and ∼ 2.99 Å are assigned to the features of Co-Al and Co-O-Al coordination bonds, respectively. Compared with Co foil and cobalt oxides, the peaks of Co-Co and Co-O-Co coordination bonds were not detected. The extended XAFS fitting shows that the average coordination numbers of Co-O, Co-Al and Co-O-Al in HCA are 3.4, 1.5 and 3.5, respectively (cf. Fig. 2C and Table S3 for details). The Wavelet transform analysis of Co K-edge extended XAFS (Fig. 2D and Fig. S3) further confirms the absence of Co-Co and Co-O-Co bonds in HCA. The lower k value of HCA than those of Co-O bonds in CoO and Co_3O_4 suggests the presence of Co-O-Al within HCA. These findings further confirmed the hyper-dispersion of cobalt cations on the millimetric support via strong metal-support interaction to form Co-O-Al or Co-Al bonds, which we think is critical to the electron spin states of coordinated cobalt atoms.

3.2. Support curvature-regulated electronic structure and spin state

XPS investigation was firstly used to identify the element composition and valence of HAC, MCA and LCA. The XPS O 1 s spectra manifest four kinds of oxygen species: Al-O (529.9 eV), Co-O (530.7 eV), oxygen defects (denoted as $O_{def.}$, 531.7 eV) and surface-absorbed oxygen (denoted as $O_{surf.}$, 532.9 eV) (Fig. S4). The fitted Co 2p spectra indicate that the cobalt species within HCA, MCA and LCA includes: Co^{3+} (779.8 eV), Co^{2+} (781.1 eV), the satellite of Co^{3+} (denoted as $Co_{sat.}^{3+}$, 784.4 eV), and the satellite of Co^{2+} (denoted as $Co_{sat.}^{2+}$, 788.6 eV) [23] (Fig. S5). The valence of Co cations for HCA, MCA and LCA can be calculated as 2.62, 2.57 and 2.65, respectively. The two sub-peaks at 73.7 eV and 74.5 eV for Al 2p spectra suggest the Al^{3+} ions in tetrahedral (Al_{Td}^{3+}) and octahedral (Al_{Oh}^{3+}) sites (Fig. S6). We think that the varied ratios of Al_{Oh}^{3+} and Al_{Td}^{3+} are probably due to the different substitutions of Co^{2+}/Co^{3+} ions at the tetrahedral and octahedral sites of γ-Al_2O_3 frameworks.

To identify the electronic structure and spin state of active cobalt centers, we collected the soft XAS spectra of HCA, MCA and LCA at their Co-L and O-K edges. The pre-edge region of O-K XAS spectra (Fig. 2E) were firstly used to probe the Co 3d – O 2p orbital hybridization effects. The much lower peak signals of 530.3 eV than 531.8 eV suggest a higher electron occupancy of t_{2g} bands than e_g bands within Co 3d orbitals [39]. The changed peak signals of 530.3 eV for HCA, MCA and LCA samples indicate that increasing the support curvature contributed to the filling of t_{2g} bands over the Co 3d – O 2p orbital hybridization. By contrast, the peak intensities of 531.8 eV remained unchanged. We think such hybridization phenomena will provide a chance to tune the filling of t_{2g} and e_g asymmetry bands and therefore, to modulate the spin states of Co 3d electrons within catalysts (as shown in Fig. 1A), which was verified by the followed Co-L edge analysis. As shown in Fig. 2F, the peak of Co-L_3 edge for LCA appeared at the highest energy position (779.37 eV), higher than those of MCA (779.27 eV) and HCA

(779.30 eV), indicating that their Co valence states followed the sequence of MCA < HCA < LCA [40]. The fitting of Co-L_3 edges (Fig. 2(G – I)) indicates the presence of four kinds of Co species: the tetrahedral and octahedral Co^{2+} ions in their high spin state (i.e., HS-Co_{Td}^{2+} and HS-Co_{Oh}^{2+}) and the octahedral Co_{Oh}^{3+} in their low and high spin state (accordingly denoted as LS-Co_{Oh}^{3+} and HS-Co_{Oh}^{3+}) [33–35]. From the quantitative fitting of XAS, the Co valence states for HCA, MCA and LCA were determined to be 2.61, 2.56 and 2.63, respectively, agreeing well with the fitting results of XPS spectra. Interestingly, there exists a positive linear correlation between the support curvature values and LS-Co_{Oh}^{3+} ratios of catalysts ($R^2 > 0.98$), while on the other hand, a negative linear relationship can be seen between the curvature and HS Co_{Oh}^{2+} ratios of catalysts ($R^2 > 0.94$) (Fig. S7(A – B)). A significant positive linear correlation was also found between the ratios of Co^{3+} species from XAS spectra and those from XPS spectra (Fig. S7C). These findings suggest a significant role of support curvature in tuning the valence, coordination structure and electron spin state of supported cobalt centers.

3.3. Catalytic decontamination and structure-activity relationship

The catalytic activities of HCA, MCA and LCA in PMS activation were systematically studied using CBZ as a model contaminant because of its wide occurrence in the aquatic environment [1]. As shown in Fig. S8, less than 4% of CBZ can be removed by the oxidation of sole PMS or the adsorption of catalysts. Comparatively, the co-presence of PMS and catalysts significantly enhanced the removal rate of CBZ (Fig. 3A). Noticeably, HCA exhibited a superior ability for PMS activation, resulting in a complete removal of CBZ within 15 min. The normalized pseudo-first-order kinetic constant by cobalt atoms (k_{nobs}) reached 770.6 min^{-1}/M_{Co}. MCA showed slightly inferior activity in PMS activation for the CBZ removal, with a corresponding k_{nobs} value of 430.6 min^{-1}/M_{Co}. By contrast, for the case of LCA, less than 62% of CBZ can be removed within 15 min, and the corresponding k_{nobs} value (133.7 min^{-1}/M_{Co}) is 5.8-times lower than that of HCA. The desirable stability of Co_2AlO_4 composite catalysts showed can be evidenced by their low concentrations of released cobalt ions (0.20 – 0.29 mg/L, much lower than the Co discharge standard in China (Co $\leq$ 1 mg/L, GB3838–2002)).

Evidently, the higher the curvature of Co_2AlO_4 composite catalysts is, the better the catalytic activities they possess, and the pseudo-first-order kinetic constant (k_{obs}) values for CBZ removal are positively linear with the curvature of catalysts (Fig. 3B). To reveal why the curvature of catalysts affected their activity, we further correlated the k_{obs} values with the microscope parameters of catalysts. As depicted in Fig. 3 (C – D), the k_{obs} values are positively associated with the ratios of LS-Co_{Oh}^{3+} within catalysts ($R^2 > 0.98$), but negatively correlated with the ratios of HS-Co_{Oh}^{2+} ($R^2 > 0.98$). As mentioned earlier, the curvature exhibited a positive linear-relationship with the ratio of LS-Co_{Oh}^{3+} ($R^2 > 0.97$), but negatively correlated with that of HS-Co_{Oh}^{2+} ($R^2 > 0.94$) (Fig. S7(A – B)). Our further investigation indicate that the BET surface areas of catalysts are proportionate to LS Co_{Oh}^{3+} contents and k_{obs} values (Fig. S7(D – E)). In addition, the specific activity (the k_{obs} value normalized to the catalyst surface area) was employed to further understand the intrinsic catalytic activity of the catalysts. However, there was no linear correlation between specific activity and Co loading (Fig. S7F). Since the higher specific surface area of catalysts is conducive to generating more LS Co_{Oh}^{3+} on their surface, we think that the high-curvature surface provided more sites to control the interactions of cobalt atoms with the support and therefore, regulated the electronic spin states of active cobalt centers within catalysts [41], which in turn, determined their catalytic activity in PMS activation.

As shown in Fig. 3E and Fig. S9, consecutive recycle experiments verify the excellent reusability and stability of HCA in the catalytic degradation of CBZ. In the duration of five reuse cycles for HCA without regeneration, the removal efficiency of CBZ can reach 100% at 20 min.
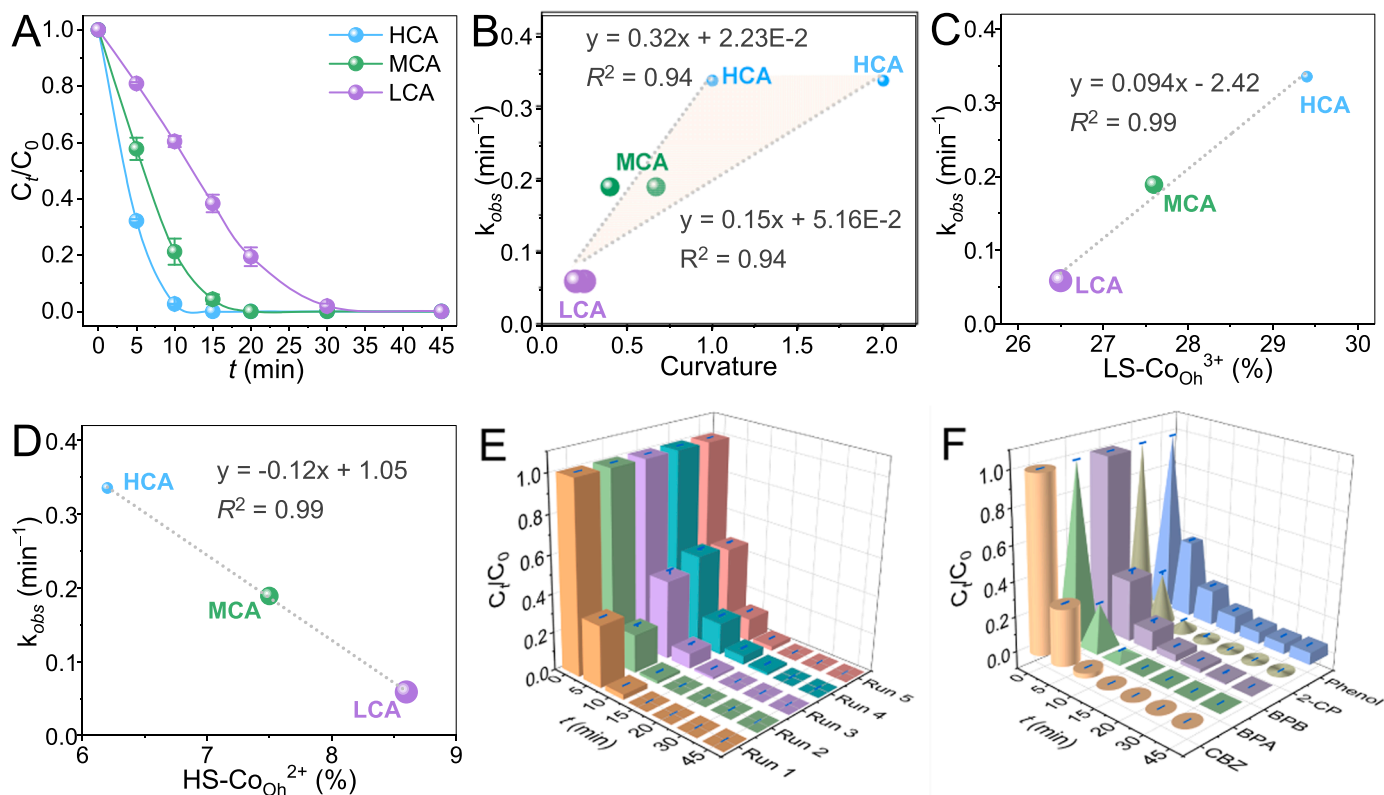
Fig. 3. Activity of macroscopic catalysts in PMS activation. (A) CBZ removal profiles by HCA, MCA and LCA activated PMS, (B – D) and the quantitative structure-activity relationships for PMS activation. (E) Reusability and catalytic stability of HCA in the concessive experiments, and (F) the performance of HCA/PMS system in the removal of various EOCs. Reaction conditions: [Catalysts] = 20 g/L, [CBZ] = [BPA] = [BPB] = [2-CP] = [Phenol] = 10 mg/L, [PMS] = 0.2 g/L, initial solution pH = 7.0, Temp. = 25 ± 1 °C.

The leached Co ions in the cycle experiments are less than 234 μg L^{-1}, much lower than the limitation of the discharge standard of Chinese groundwater (1 mg L^{-1}). We attribute the catalytic stability of HCA to its stable structure and surface property over PMS activation (refer to Fig. S10). Moreover, HCA demonstrated a universal applicability of catalyzing PMS to remove other EOCs, i.e., BPA, BPB, 2-CP, and phenol (Fig. 3F). Clearly, BPA followed a similar removal profile of CBZ with its removal efficiency being 100% in less than 15 min. In the same duration, 95.98% of BPB, 99.10% of 2-CP, and 90.27% of phenol can be also degraded, and the corresponding k_{obs} values were calculated to be 0.22, 0.28 and 0.16 min^{-1}, respectively. Additionally, the total cost of materials and energy consumption for the large-scale production of such spin catalysts can be lower than $1.87 × 10^{-2}$/g (1.37 ×10^{-1} RMB/g) (cf. Text S7 and Table S4), much lower than the commercial PMS activators [32]. Moreover, HCA shows a comparable performance with other catalysts towards PMS activation for CBZ removal (refer to Table S5). Generally, these findings suggest the high stability and a great potential of millimetric HCA in catalytically removing a wide spectrum of micropollutants.

3.4. Catalytic mechanism of spin state-tailored millimetric Co oxides

Using HCA as a model catalyst, we used theoretical calculations and experimental results to uncover how PMS was activated by the spin state-tailored macroscopic cobalt catalyst and the pathways of generating dominant reactive species. XPS investigations suggest that the content of O$_{def.}$ for used HCA increased from 37.8% to 40.8% during the PMS activation (Figs. S4A and S11A). The oxidation state of cobalt in HCA was slightly increased after reacting with PMS (from 2.62 to 2.69) (Figs. S5A and S11B). Nevertheless, the ratios of Al$_{Oh}^{3+}$ and Al$_{Td}^{3+}$ changed significantly (Figs. S6A and S11C), due to the varied occupations of

cobalt ions immobilized in the Al$_2$O$_3$ support during the PMS activation. These findings imply that there probably exists a new mechanism for PMS activation.

(A – C) SO$_5^{2-}$ adsorption calculation: (A) calculated HOMO and LUMO, (B) side and top view of Co$_2$AlO$_4$ surfaces with surface Co$_{4c}$(Oh) and Co$_{3c}$(Td) as potential active sites for the SO$_5^{2-}$ adsorption, (C) optimized geometries for SO$_5^{2-}$ co-adsorbed by Co$_{4c}$(Oh) and Co$_{3c}$(Td) or only by Co$_{3c}$(Td), indicated by the green and blue circle in (B, bottom). S, O and Co are shown as yellow, red and blue balls. (D – F) Calculated data for electronics and reaction profile: Projected *d*-DOS for (D) Co$_{3c}$(Td) and (E) Co$_{4c}$(Oh) with Fermi energy as the reference (green dash lines). (F) Relative energy for reaction intermediate states from PMS to generate SO$_4^{•-}$ and O*. The EPR spectra of DMPO$^{•}$-OH/SO$_4^-$ adducts (G), TMEP-^{1}O$_2$ adducts (H) and DMPO$^{•}$-O$_2^-$ adducts (I) in the HCA/PMS system ([DMPO] = 100 mM, [TEMP] = 100 mM, [HCA powders] = 0. 25 g/L, [PMS] = 0.2 g/L). (J – L) The effects of scavengers on CBZ removal by HCA, MCA and LCA activated PMS ([Catalysts] = 20 g/L, [CBZ] = 10 mg/L, [PMS] = 0.2 g/L, initial solution pH = 7.0, Temp. = 25 ± 1 °C).
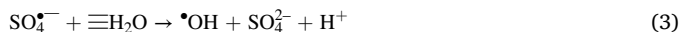
Previous studies indicate that the deprotonation of terminal O-H group within PMS can affect the O-O bond cleavage and the production of free radicals and other reactive species [42,43]. Our XPS investigations (Figs. S4A, S5A, S6A and S11) imply that for current system, the deprotonation of HSO$_5^-$ into SO$_5^{2-}$ probably occurred prior to the formation of free radicals and reactive oxygen species. For example, from the high-resolution XPS spectra of Al 2p and Co 2p, it can be calculated that the reduced ratio of Al-O bonds is about 3.29%, 5 times higher than the increased ratio of Co-O bonds (about 0.63%). This finding suggests an oxygen loss on the active interface of catalyst surface during the PMS activation, which we think is due to the combined interfacial effects of the cleavage of polar O-H bond within HSO$_5^-$ and

the subsequent reaction of oxygen with the hydrogen proton [43]. From the exposed active facet of HCA (Fig. 1) and spin-polarized calculations via DFT, it was found that HCA-induced PMS activation needed to inject one electron to the catalyst and potentially coupled with the proton released from HSO_5^- (to form deprotonated SO_5^{2-}). Thus, as indicated in Fig. 4A, both HOMO (highest occupied molecular orbital) and LUMO (lowest unoccupied molecular orbital) have been plotted, from which the molecular orbitals are dominated by the O-O terminal of deprotonated SO_5^{2-}. As revealed by optimized geometries, the SO_5^{2-} with the O-O terminal can be adsorbed by lowly coordinated Co-site via Co-O bonding. As shown in Fig. 4B, the tetrahedral (Td) and octahedral (Oh) cobalt cations on catalyst surface exist with their dangling bonds, labelled as $Co_{3c}(Td)$ and $Co_{4c}(Oh)$, respectively. Consequently, SO_5^{2-} can be potentially adsorbed over these sites, as labelled by the green and blue dash circles in the top view (see Fig. 4B), over which SO_5^{2-} can be co-adsorbed by $Co_{4c}(Oh)$ and $Co_{3c}(Td)$ in the green circle or solely adsorbed by $Co_{3c}(Td)$. Due to the oxidation capacity of SO_5^{2-}, the electron transfer is transferred from surface Co sites to SO_5^{2-}, strongly determined by the adsorption between SO_5^{2-} and the dangling bonds of $Co_{3c}(Td)$ and $Co_{4c}(Oh)$. The fully optimized geometries are presented in Fig. 4C, with the former being energetically favorable by -0.93 eV. This difference vividly highlights the value for synergetic role between $Co_{3c}(Td)$ and $Co_{4c}(Oh)$ sites.

Therefore, the density of states (DOS) has been calculated and projected with *d*-orbitals to understand the reactivity difference between $Co_{3c}(Td)$ and $Co_{4c}(Oh)$ sites. As highlighted by the red rectangles, the states around Fermi energy show remarkable difference (Figs. 4D and 4E). Specifically, the $Co_{3c}(Td)$ site shows weak states for both spin up and spin down, while the $Co_{4c}(Oh)$ site presents strong occupied spin up states and unoccupied spin down states. As discussed above, strong capacity to accept and donate electrons is beneficial for the adsorption and conversion for SO_5^{2-}. As indicated by DOS profiles, only $Co_{4c}(Oh)$ presents such capacity, which explains the difference of SO_5^{2-} adsorption over the green and blue circles in Fig. 4B.

Then, we performed the analysis of SO_5^{2-} conversion into reactive radicals and nonradicals. As depicted by the energy profile shown in Fig. 4F, SO_5^{2-} experienced successive processes of adsorption, O-O dissociation and $SO_4^{\bullet-}$ production. As a result, three intermediate states have been involved, as labelled in the figure. Specifically, the pink and blue lines show their relative energies of these states when it is catalyzed by joint $Co_{4c}(Oh)$ and $Co_{3c}(Td)$ or solely by $Co_{3c}(Td)$. As derived from this result, the potential-determining step comes from the production of $SO_4^{\bullet-}$, requesting an energy input of 2.46 eV and 4.42 eV, respectively. Clearly, the joint reaction path is favorable for generating $SO_4^{\bullet-}$ and reactive oxygen (O*), which the latter can react with HSO_5^- or adsorbed SO_5^{2-} to form $^1O_2$ and $O_2^{\bullet-}$ via Reaction (1) and (2) [42,44–46].

$$O^* + HSO_5^- \rightarrow {}^1O_2 + SO_4^{2-} + H^+ \qquad (1)$$

$$2\,O^* + \equiv SO_5^{2-} \rightarrow O_2^{\bullet-} + SO_5^{\bullet-} \qquad (2)$$

$$SO_4^{\bullet-} + \equiv H_2O \rightarrow {}^\bullet OH + SO_4^{2-} + H^+ \qquad (3)$$

The electron paramagnetic resonance (EPR) characterizations and quenching experiments were carried out to confirm the above reactive species. As shown in Fig. 4(G – I), compared with the EPR spectra of sole HCA or PMS, significantly higher intensities of DMPO$^\bullet$-OH/SO_4^- adducts, TMEP-$^1O_2$ adducts and DMPO$^\bullet$-O_2^- adducts were observed for the combination of HCA and PMS, suggesting the simultaneous formation of $SO_4^{\bullet-}$, $^\bullet$OH, $^1O_2$ and $O_2^{\bullet-}$, which is due to the PMS activation by HCA. Note that our DFT calculations indicate that generating $SO_4^{\bullet-}$ and $^\bullet$OH simultaneously at the HCA catalytic interface during PMS activation is thermodynamically prohibited. We think that the production of $^\bullet$OH is probably due to the reaction of with the adsorbed H_2O ($\equiv H_2O$) on catalyst surface via Reaction (3) [46]. To better verify the above reactive species, we carefully designed the quenching experiments and selected the concentrations of quenchers (refer to Table S6). Firstly, EtOH was

selected as a typical quencher for both $SO_4^{\bullet-}$ and $^\bullet$OH (inert to $^1O_2$ and $O_2^{\bullet-}$), while TBA could serve as a specific $^\bullet$OH quencher according to their second-order reaction rate constants with $SO_4^{\bullet-}$, $^\bullet$OH, $^1O_2$ and $O_2^{\bullet-}$ [46]. As depicted in Fig. 4J, 0.1 M EtOH greatly inhibited the removal of CBZ, suggesting the major role of $SO_4^{\bullet-}$ and/or $^\bullet$OH in the HCA/PMS system. Nevertheless, the lower inhibition of 0.5 M TBA than 0.1 M EtOH for the HCA/PMS system can exclude the dominant role of $^\bullet$OH in CBZ removal, because both 0.5 M TBA and 0.1 M EtOH have a comparable first-order reaction rate constant of about $1.9 \times 10^8\ s^{-1}$ with $^\bullet$OH [46]. Since the first-order reaction rate constant of 1 mM HD (a commonly used $^1O_2$ scavenger but inert to $O_2^{\bullet-}$) with is comparable to that of 0.1 M EtOH ($2.5 \times 10^6\ s^{-1}$ vs $(1.6 - 7.7) \times 10^6\ s^{-1}$) [46], the nearly complete inhibition of 1 mM HD suggests the important contribution of $^1O_2$ to CBZ degradation. Even though BQ (commonly used as a scavenger of $O_2^{\bullet-}$) can react with $SO_4^{\bullet-}$, $^\bullet$OH, and $^1O_2$ simultaneously [46], the inhibition of 1 mM BQ is much lower than that of 1 mM HD despite their comparable first-order reaction rate constants with $^1O_2$ ($6.6 \times 10^4\ s^{-1}$ vs $3.8 \times 10^4\ s^{-1}$). This implies a negligible effect of $O_2^{\bullet-}$ on CBZ removal. Although HD and BQ may decompose PMS in buffering system [29,47,48], the decomposition or activation of PMS induced by low concentration of 1 mM HD (or BQ) without buffering substances can be neglected based on our previous work [21]. Therefore, the inhibition of 1 mM HD (or BQ) to CBZ degradation can be ascribed to their quenching effects on the radical/nonradical species. In all, among the identified reactive species, $SO_4^{\bullet-}$ and $^1O_2$ are the dominate oxidants for the oxidation of CBZ by the HCA/PMS system.

3.5. Catalytic degradation pathways and product toxicity

The catalytic degradation pathways of CBZ by the three catalysts were verified by chemical quenching experiments and high-performance liquid chromatography-mass spectrometry system (refer to Fig. S12 and Table S7). As shown in Fig. 4(J – L), the CBZ degradation was significantly suppressed by 0.1 M EtOH, suggesting the dominant role of radical oxidation in CBZ degradation in the three HCA/PMS, MCA/PMS and LCA/PMS systems. Comparatively, the inhibition of 0.5 M TBA is much lower than that of 0.1 M EtOH, verifying that the catalytic degradation of CBZ by the three catalysts is mainly due to the oxidation of $SO_4^{\bullet-}$ radicals. Almost complete inhibition in the removal of CBZ (inhibition rate > 99%) was observed after adding 1 mM HD into the catalytic reaction systems. This implies the participation of $^1O_2$ in the CBZ degradation. The much stronger inhibition of 1 mM HD than 1 mM BQ suggests a more important role of $^1O_2$ than $O_2^{\bullet-}$ in the CBZ degradation [46]. The inhibition rates caused by EtOH slightly decreased with the curvature of catalyst supports decreased (from 95.7% of HCA to 94.3% of MCA, and then to 87.5% of LCA, Table S6). By contrast, when the support curvature values were decreased, an increased inhibition ability of TBA (from 53.6% to 58.4%) and BQ (from 68.6% to 88.2%) was observed. This finding indicates that decreasing the support curvature is probably favorable for the formation of $^\bullet$OH and $O_2^{\bullet-}$ (especially for $O_2^{\bullet-}$). However, the formation of more amount of $O_2^{\bullet-}$ could worsen the oxidation degradation of CBZ. This is because the estimated second-order reaction rate constant of $O_2^{\bullet-}$ with CBZ ($< 10^7$ $M^{-1}\ s^{-1}$) is much lower than those of $SO_4^{\bullet-}$ ($8.8 \times 10^9\ M^{-1}\ s^{-1}$) and $^\bullet$OH ($1.92 \times 10^9\ M^{-1}\ s^{-1}$) [49,50]. Despite the support curvature-regulated reactive radicals/species, the catalytic degradation of CBZ by the three catalysts mainly relies on $SO_4^{\bullet-}$ and $^1O_2$.

The product distributions were studied to further probe the catalytic degradation pathways of CBZ controlled by the catalyst spin-states. As shown in Fig. 5(A – C) and Table S7, the three systems shared similar transformation products (marked as their molecule weight), except for the absence of product C223 in the LCA/PMS system. The main difference lies in the content of each product. The proportions of top-ranked product C252 in the HCA/PMS, MCA/PMS and LCA/PMS systems are 77.5%, 79.1% and 81.1%, respectively, more than seven times higher than those of the second-ranked C250 (6.28–10.67%). The first-three
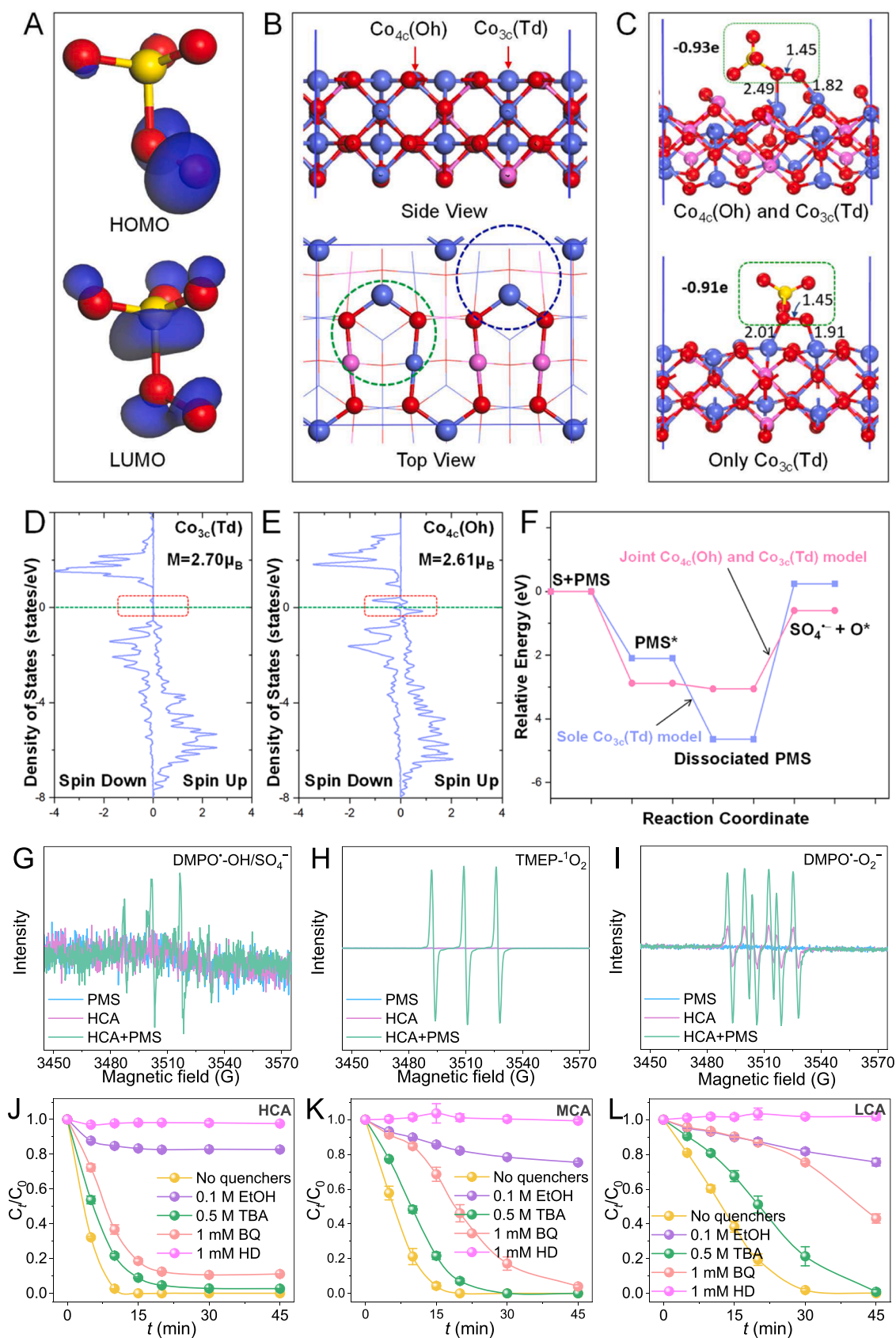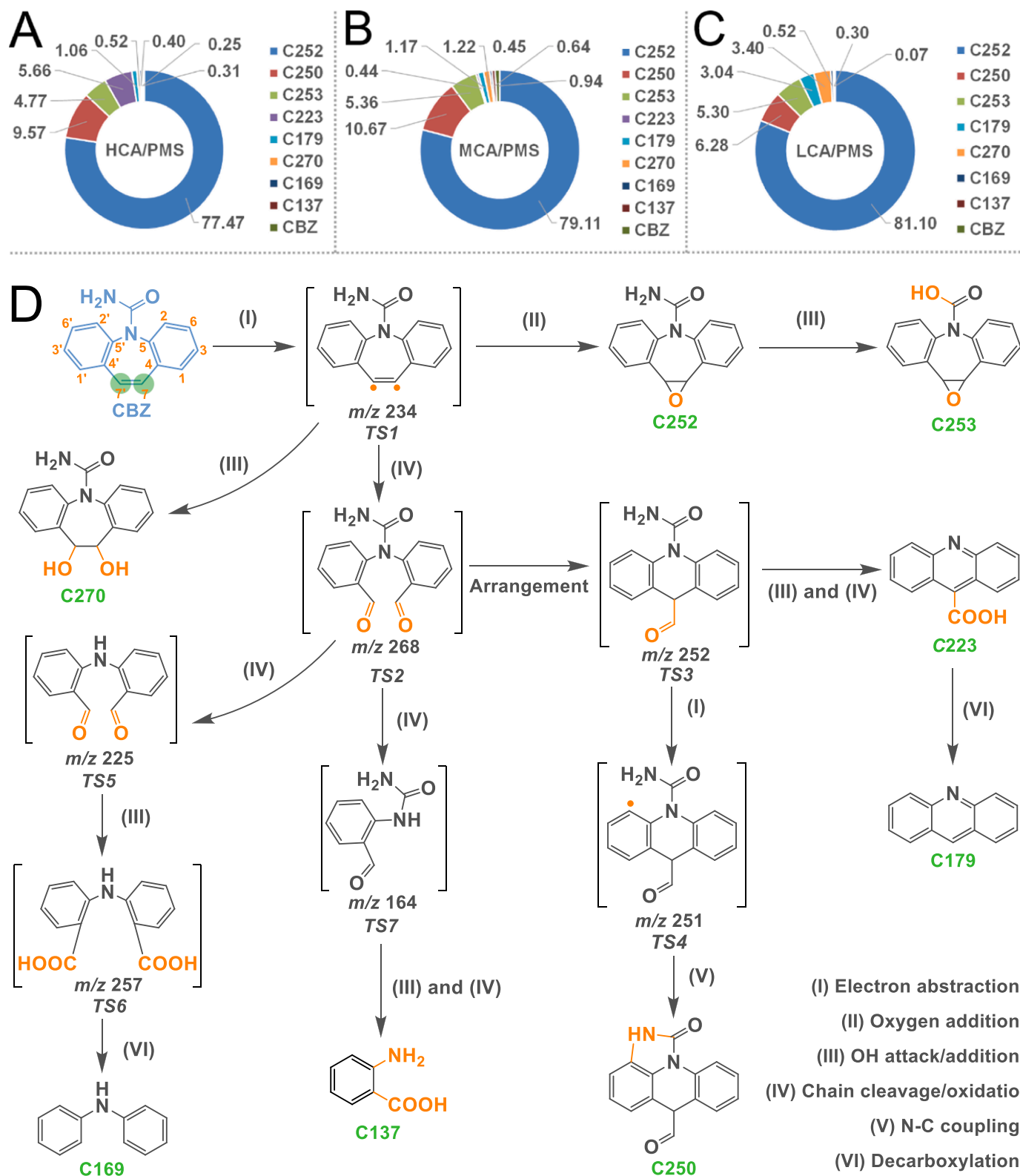
Fig. 4. Catalytic mechanism analysis on PMS activation for the formation of reactive species.

Fig. 5. Catalytic degradation pathways for target EOC. (A – C) The distributions of CBZ oxidation products generated in the HCA/PMS, MCA/PMS and LCA/PMS systems, and (D) the proposed catalytic oxidation pathways of CBZ shared by the three systems.

important products of C252, C250 and C253 shared in the three catalytic systems suggest that the CBZ degradation was controlled by the same reactive radicals/species ($SO_4^{•-}$ and $^1O_2$). Obviously, the curvature-regulated spin-states slightly changed the types of products but moderately affected their contents. The varied product proportions probably

result from the changeable contents of reactive radicals, which intrinsically relies on the spin-states of catalysts.

As illustrated in Fig. 5D, the catalytic reaction pathways for CBZ degradation include electron abstract, oxygen addition, chain cleavage, •OH attack/addition, N-C coupling and decarboxylation. The first step

for the CBZ catalytic degradation was triggered by radicals-induced single electron transfer (SET) process, leading to a transition species (*TS1*, *m/z* 234) via the abstraction of one electron from the olefinic double bond of CBZ (i.e., the C7 and C7' sites, marked with green circles) because of its relatively high Fukui index [51,52]. Then, the followed reaction pathways proceeded: (1) The oxygen addition on *TS1* generated C252, and the •OH attack/addition on C252 produced C253. The •OH radical attack on *TS1* resulted in C270. The overwhelming contents of C252 (> 77%) indicate that the SET reaction is the primary pathway for the CBZ catalytic oxidation. (2) The chain cleavage and oxygen addition of *TS1* resulted in one transition species of *TS2*, which was converted into another transition species of *TS3* via arrangement. The radicals-mediated electron abstraction from *TS3* (generating *TS4*) and the N-C coupling on *TS4* generated C250. (3) The combined N-C bond cleavage and •OH addition on *TS3* led to the formation of C223, which was further transformed into C179 via decarboxylation. (4) The N-C cleavage of *TS2* (to form *TS5*), the •OH addition on *TS5* (to produce *TS6*) and the decarboxylation of *TS6* synergistically generated C169, while two successive N-C cleavage reactions coupled with the •OH addition on *TS7* (from *TS2*) resulted in C137. The abovementioned pathways could occur in parallel at different levels, which is due to the changeable reactive species dominated by the spin-states of catalysts.

Fig. 6 and Table S8 show the estimated toxicity values of bioaccumulation factor (BAF), mutagenicity, *Daphnia magna* LC50, and *oral rat* LD50 for the CBZ degradation by the three catalysts. Based on the ratios of products, we normalized toxicity indexes and calculated the total toxicity of all products in each system (cf. Table S9). Besides C179 and C169, the rest of products have lower BAF values than that of parent CBZ (Fig. 6A). The normalized BAF values of all the CBZ degradation products in the HCA/PMS, MCA/PMS and LCA/PMS system are 17.7, 17.9 and 20.3, respectively. Obviously, the HCA/PMS system showed the greatest capacity of reducing the bioaccumulation potential of oxidation products. As calculated, the parent CBZ is a mutagenic pollutant due to its higher mutagenicity value. Although the products of C223, C270, C169 and C137 are not mutagenic, the products of C252, C250, C253 and C179 have higher mutagenicity values than that of CBZ (Fig. 6B). The normalized total mutagenicity values of all the products are higher than that of parent CBZ (Fig. 6B), suggesting the potential mutagenicity risk of products generated in the three oxidation systems. The oxidation products of CBZ have greater LC50 values than that of parent CBZ (Fig. 6C), suggesting the positive role of the HCA/PMS, MCA/PMS and LCA/PMS oxidation systems in lowering the acute toxicity to *Daphnia magna*. The *Oral rat* LD50 values imply a slightly enhanced acute toxicity for the CBZ degradation by the three oxidation systems (Fig. 6D). In all, the varied products distributions caused by spin state-regulated Co$_2$AlO$_4$ catalysts slightly affected the BAF, mutagenicity, and the acute toxicity for the CBZ oxidation degradation.

4. Conclusion

In summary, we report a feasible and scalable method of developing cost-effective millimetric Co-based nanocatalysts with regulated electron configurations and spin states via constructing bonded Co-O-Al ligands on γ-Al$_2$O$_3$ millispheres. Tuning the support curvature of millimetric catalysts has shown to be effective in modulating the coordination configurations of cobalt centers and their electronic spin states. The spin states-regulated tetrahedral and octahedral cobalt centers with macroscopic catalyst exhibited a synergistic role in PMS activation and formation of reactive species, thus changing the distributions of pollutant degradation products and their toxicity. The catalysts with more LS-Co^{3+} species but less HS-Co^{2+} species were found to possess a superior activity in PMS activation and simultaneously exhibited a
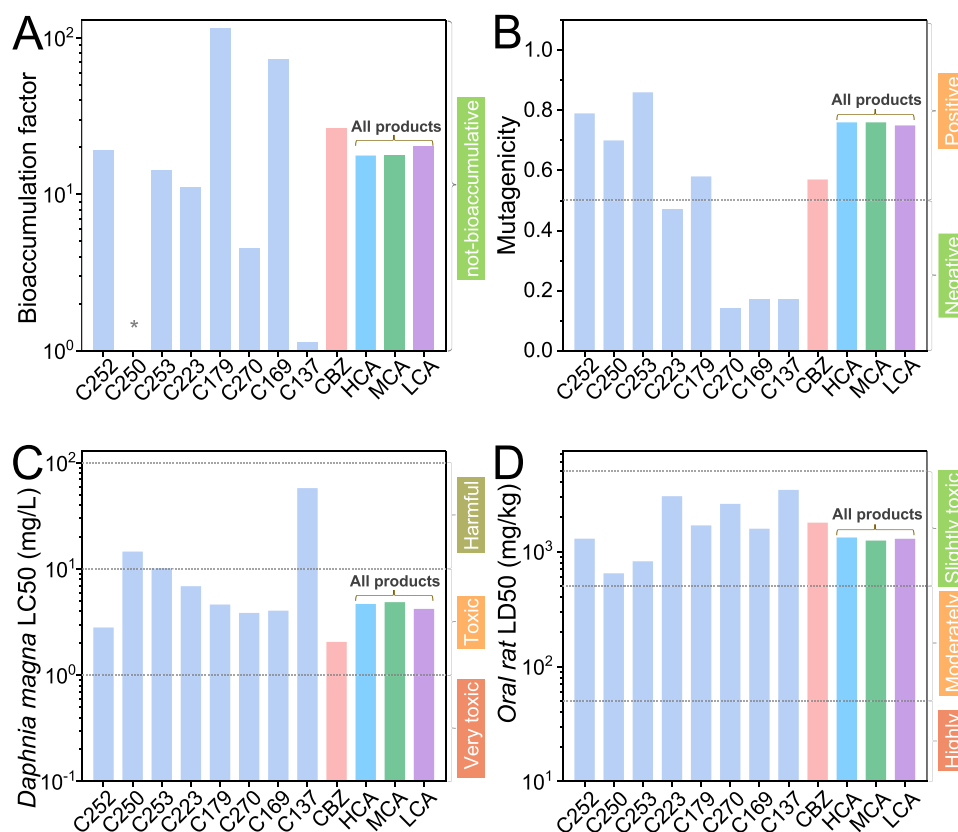
Fig. 6. Analysis on the changed toxicity of degradation products. (A) The predicted bioaccumulation factor, (B) mutagenicity, (C) *Daphnia magna* LC50, (D) *Oral rat* LD50 of parent CBZ and its oxidation products, as well as the corresponding normalized total value for all the products of CBZ formed in the HCA/PMS, MCA/PMS and LCA/PMS systems. * means the data are not available.

lasting reusability and catalytic stability for their consecutive reuse. Moreover, the millimetric spin catalysts are cheaper than commercial Co-based powder catalysts. This work will spark more interest in the design of macroscopic non-precious metal catalysts with versatile electronic configurations and functions in their mass production scale for advanced catalysis applications.

CRediT authorship contribution statement

Jia-Cheng E. Yang: Conceptualization, Visualization, Writing – original draft, Writing – review & editing, Funding acquisition. **Min-Ping Zhu**: Conceptualization, Investigation, Methodology, Formal analysis, Visualization, Writing – original draft. **Daqin Guan**: Methodology, Writing – review & editing. **Baoling Yuan** and **Darren Delai Sun**: Writing – review & editing. **Chenghua Sun**: Supervision, Methodology, Writing – review & editing. **Ming-Lai Fu**: Supervision, Resources, Writing – review & editing, Funding acquisition.

Declaration of Competing Interest

The authors declare that they have no known competing financial interests or personal relationships that could have appeared to influence the work reported in this paper.

Data availability

Data will be made available on request.

Acknowledgements

Appendix A. Supporting information

Supplementary data associated with this article can be found in the online version at doi:10.1016/j.apcatb.2023.123466.

References

[1] J.L. Wilkinson, A.B.A. Boxall, D.W. Kolpin, K.M.Y. Leung, R.W.S. Lai, C. Galbán-Malagón, A.D. Adell, J. Mondon, M. Metian, R.A. Marchant, A. Bouzas-Monroy, A. Cuni-Sanchez, A. Coors, P. Carriquiriborde, M. Rojo, C. Gordon, M. Cara, M. Moermond, T. Luarte, V. Petrosyan, Y. Perikhanyan, C.S. Mahon, C.J. McGurk, T. Hofmann, T. Kormoker, V. Iniguez, J. Guzman-Otazo, J.L. Tavares, F. Gildasio De Figueiredo, M.T.P. Razzolini, V. Dougnon, G. Gbaguidi, O. Traoré, J.M. Blais, L. E. Kimpe, M. Wong, D. Wong, R. Nthantcho, J. Pizarro, G. Ying, C. Chen, M. Páez, J. Martínez-Lara, J. Otamonga, J. Poté, S.A. Ifo, P. Wilson, S. Echeverría-Sáenz, N. Udikovic-Kolic, M. Milakovic, D. Fatta-Kassinos, L. Ioannou-Ttofa, V. Belušová, J. Vymazal, M. Cárdenas-Bustamante, B.A. Kassa, J. Garric, A. Chaumot, P. Gibba, I. Kunchulia, S. Seidensticker, G. Lyberatos, H.P. Halldórsson, M. Melling, T. Shashidhar, M. Lamba, A. Nastiti, A. Supriatin, N. Pourang, A. Abedini, O. Abdullah, S.S. Gharbia, F. Pilla, B. Chefetz, T. Topaz, K.M. Yao, B. Aubakirova, R. Beisenova, L. Olaka, J.K. Mulu, P. Chatanga, V. Ntuli, N.T. Blama, S. Sherif, A. Z. Aris, L.J. Looi, M. Niang, S.T. Traore, R. Oldenkamp, O. Ogunbanwo, M. Ashfaq, M. Iqbal, Z. Abdeen, A.O. Dea, J.M. Morales-Saldaña, M. Custodio, H. de la Cruz, I. Navarrete, F. Carvalho, A.B. Gogra, B.M. Koroma, V. Cerkvenik-Flajs, M. Gombač, M. Thwala, K. Choi, H. Kang, J.L.C. Ladu, A. Rico, P. Amerasinghe, A. Sobek, G. Horlitz, A.K. Zenker, A.C. King, J. Jiang, R. Kariuki, M. Tumbo, U. Tezel, T.T. Onay, J.B. Lejju, Y. Vystavna, Y. Vergeles, H. Heinzen, A. Pérez-Parada, D.B. Sims, M. Figy, D. Good, C. Teta, Pharmaceutical pollution of the world's rivers, P. Natl. Acad. Sci. USA 119 (2022) e2113947119.

[2] K.M.M. Pärnänen, C. Narciso-da-Rocha, D. Kneis, T.U. Berendonk, D. Cacace, T. T. Do, C. Elpers, D. Fatta-Kassinos, I. Henriques, T. Jaeger, A. Karkman, J. L. Martinez, S.G. Michael, I. Michael-Kordatou, K.O. Sullivan, S. Rodriguez-Mozaz, T. Schwartz, H. Sheng, H. Sørum, R.D. Stedtfeld, J.M. Tiedje, S.V.D. Giustina, F. Walsh, I. Vaz-Moreira, M. Virta, C.M. Manaia, Antibiotic resistance in European

[3] P.Y. Nguyen, G. Carvalho, M.A.M. Reis, A. Oehmen, A review of the biotransformations of priority pharmaceuticals in biological wastewater treatment processes, Water Res 188 (2021), 116446.

[4] J. Li, Z. Xiong, Y. Yu, X. Wang, H. Zhou, B. Huang, Z. Wu, C. Yu, T. Chen, Z. Pan, G. Yao, B. Lai, Efficient degradation of carbamazepine by electro-Fenton system without any extra oxidant in the presence of molybdate: the role of slow release of iron ions, Appl. Catal. B: Environ. 298 (2021), 120506.

[5] S. Wang, J. Chen, Y. Sun, B. Sun, J. Qiao, X. Guan, Roles of MnO_2 colloids and Mn (III) during the oxidation of organic contaminants by permanganate, Environ. Sci. Technol. 57 (2023) 997–1005.

[6] Z. Zheng, J. Min, X. Wang, C.W. Lung, K. Shih, I.M.C. Lo, Directional separation of highly reductive electrons to the reactive center in a magnetic S-scheme $ZnFe_2O_4$/A-MoS_2 heterojunction for enhanced peroxymonosulfate activation toward pharmaceuticals and personal care product removal, Environ. Sci. Technol. 57 (2023) 8414–8425.

[7] B.C. Hodges, E.L. Cates, J. Kim, Challenges and prospects of advanced oxidation water treatment processes using catalytic nanomaterials, Nat. Nanotechnol. 13 (2018) 642–650.

[8] J. Lee, U. von Gunten, J. Kim, Persulfate-based advanced oxidation: Critical assessment of opportunities and roadblocks, Environ. Sci. Technol. 54 (2020) 3064–3081.

[9] W. Ren, C. Cheng, P. Shao, X. Luo, H. Zhang, S. Wang, X. Duan, Origins of electron-transfer regime in persulfate-based nonradical oxidation processes, Environ. Sci. Technol. 56 (2022) 78–97.

[10] Z. Guo, Y. Si, W. Xia, F. Wang, H. Liu, C. Yang, W. Zhang, W. Li, Electron delocalization triggers nonradical Fenton-like catalysis over spinel oxides, P. Natl. Acad. Sci. USA 119 (2022), e2093360177.

[11] X. Li, X. Huang, S. Xi, S. Miao, J. Ding, W. Cai, S. Liu, X. Yang, H. Yang, J. Gao, J. Wang, Y. Huang, T. Zhang, B. Liu, Single cobalt atoms anchored on porous N-doped graphene with dual reaction sites for efficient Fenton-like catalysis, J. Am. Chem. Soc. 140 (2018) 12469–12475.

[12] M. Huang, Y. Li, C. Zhang, C. Cui, Q. Huang, M. Li, Z. Qiang, T. Zhou, X. Wu, H. Yu, Facilely tuning the intrinsic catalytic sites of the spinel oxide for peroxymonosulfate activation: from fundamental investigation to pilot-scale demonstration, P. Natl. Acad. Sci. USA 119 (2022), e2092285177.

[13] Z.Y. Guo, C.X. Li, M. Gao, X. Han, Y.J. Zhang, W.J. Zhang, W.W. Li, Mn-O covalency governs the intrinsic activity of Co-Mn spinel oxides for boosted peroxymonosulfate activation, Angew. Chem. Int. Ed. 60 (2021) 274–280.

[14] J. Yu, T. Zeng, H. Wang, H. Zhang, Y. Sun, L. Chen, S. Song, L. Li, H. Shi, Oxygen-defective MnO_2-x rattle-type microspheres mediated singlet oxygen oxidation of organics by peroxymonosulfate activation, Chem. Eng. J. 394 (2020), 124458.

[15] M. Zhu, J.E. Yang, D. Guan, B. Yuan, X. Duan, D.D. Sun, C. Sun, S. Wang, M. Fu, Surface Al and Co coordination for peroxymonosulfate activation: Identification and mechanism, Appl. Catal. B: Environ. 329 (2023), 122570.

[16] C. Zhao, B. Liu, X. Li, K. Zhu, R. Hu, Z. Ao, J. Wang, A. Co–Fe, Prussian blue analogue for efficient Fenton-like catalysis: the effect of high-spin cobalt, Chem. Commun. 55 (2019) 7151–7154.

[17] M. Li, G. Ren, W. Yang, F. Wang, N. Ma, X. Fan, Q. Pan, Modulation of high-spin Co (II) in Li/Co-MOFs as efficient Fenton-like catalysts, Inorg. Chem. 60 (2021) 12405–12412.

[18] L. Pan, M. Ai, C. Huang, L. Yin, X. Liu, R. Zhang, S. Wang, Z. Jiang, X. Zhang, J. Zou, W. Mi, Manipulating spin polarization of titanium dioxide for efficient photocatalysis, Nat. Commun. 11 (2020) 418.

[19] C. Zhu, L. Lu, Q. Fang, S. Song, B. Chen, Y. Shen, Unveiling spin state-dependent micropollutant removal using single-atom covalent triazine framework, Adv. Funct. Mater. 33 (2023) 4704–4711.

[20] J. Miao, Y. Zhu, J. Lang, J. Zhang, S. Cheng, B. Zhou, L. Zhang, P.J.J. Alvarez, M. Long, Spin-state-dependent peroxymonosulfate activation of single-atom M-N moieties via a radical-free pathway, ACS Catal. 11 (2021) 9569–9577.

[21] M. Zhu, J.E. Yang, X. Duan, D. Zhang, S. Wang, B. Yuan, M. Fu, Interfacial $CoAl_2O_4$ from ZIF-67@γ-Al_2O_3 pellets toward catalytic activation of peroxymonosulfate for metronidazole removal, Chem. Eng. J. 397 (2020), 125339.

[22] L. Zhu, J. Ji, J. Liu, S. Mine, M. Matsuoka, J. Zhang, M. Xing, Designing 3D-MoS_2 sponge as excellent cocatalysts in advanced oxidation processes for pollutant control, Angew. Chem. Int. Ed. 59 (2020) 2–11.

[23] S. Mo, Q. Zhang, Q. Ren, J. Xiong, M. Zhang, Z. Feng, D. Yan, M. Fu, J. Wu, L. Chen, D. Ye, Leaf-like Co-ZIF-L derivatives embedded in Co_2AlO_4/Ni foam from hydrotalcites as monolithic catalysts for toluene abatement, J. Hazard. Mater. 364 (2019) 571–580.

[24] Y. Li, X. Yan, X. Hu, R. Feng, M. Zhou, Trace pyrolyzed ZIF-67 loaded activated carbon pellets for enhanced adsorption and catalytic degradation of Rhodamine B in water, Chem. Eng. J. 375 (2019), 122003.

[25] Y. Wang, S. Hui, S. Zhan, R. Djellabi, J. Li, X. Zhao, Activation of peroxymonosulfate by novel Pt/Al_2O_3 membranes via a nonradical mechanism for efficient degradation of electron-rich aromatic pollutants, Chem. Eng. J. 381 (2020), 122563.

[26] J. Liang, K. Gao, A. Zhou, Y. Fang, S. Su, L. Fu, M. Sun, X. Duan, Long-lasting performance of high-flux perovskite membrane for catalytic degradation of organic pollutants, Appl. Catal. B: Environ. 327 (2023), 122440.

[27] K. Wei, X. Cao, W. Gu, P. Liang, X. Huang, X. Zhang, Ni-induced C-Al_2O_3-framework (Ni CAF) supported core-multishell catalysts for efficient catalytic ozonation: a structure-to-performance study, Environ. Sci. Technol. 53 (2019) 6917–6926.

[28] X. Kong, S. Garg, M. Mortazavi, J. Ma, T.D. Waite, Heterogenous iron oxide assemblages for use in catalytic ozonation: reactivity, kinetics, and reaction mechanism, Environ. Sci. Technol. (2023), https://doi.org/10.1021/acs.est.2c07319.

[29] B. Li, H. Xu, Y. Liu, Y. Liu, Y. Xu, S. Zhang, Unveiling the structure–activity relationships of ofloxacin degradation by Co_3O_4-activated peroxymonosulfate: From microstructures to exposed facets, Chem. Eng. J. 467 (2023), 143396.

[30] Q. Pan, Q. Gao, G. Gao, M. Liu, B. Han, K. Xia, C. Zhou, Composition-engineered $LaCoO_3$-based monolithic catalysts for easily operational and robust peroxymonosulfate activation, Chem. Eng. J. 424 (2021), 130574.

[31] D. Liu, Z. Su, B. Han, K. Xia, C. Zhou, Q. Gao, Cobalt–aluminum oxide clusters-embedded γ-Al_2O_3 nanosheets for peroxymonosulfate activation: Interfacial pH-buffering property to eliminate cobalt leaching and boost the catalytic activity, Appl. Catal. B: Environ. (2023), 122555.

[32] M. Zhu, J.E. Yang, X. Duan, S. Wang, D.D. Sun, B. Yuan, M. Fu, Engineered Co_2AlO_4/$CoAl_2O_4$@Al_2O_3 monolithic catalysts for peroxymonosulfate activation: Co^{3+}/Co^{2+} and O_{Defect}/$O_{Lattice}$ ratios dependence and mechanism, Chem. Eng. J. 409 (2021), 128162.

[33] C.F. Chang, Z. Hu, H. Wu, T. Burnus, N. Hollmann, M. Benomar, T. Lorenz, A. Tanaka, H.J. Lin, H.H. Hsieh, C.T. Chen, L.H. Tjeng, Spin blockade, orbital occupation, and charge ordering in $La_{1.5}Sr_{0.5}CoO_4$, Phys. Rev. Lett. 102 (2009).

[34] D. Guan, J. Zhou, Z. Hu, W. Zhou, X. Xu, Y. Zhong, B. Liu, Y. Chen, M. Xu, H.J. Lin, C.T. Chen, J.Q. Wang, Z. Shao, Searching general sufficient-and-necessary conditions for ultrafast hydrogen-evolving electrocatalysis, Adv. Funct. Mater. 29 (2019), 1900704.

[35] A.M. Hibberd, H.Q. Doan, E.N. Glass, F.M.F. de Groot, C.L. Hill, T. Cuk, Co polyoxometalates and a Co_3O_4 thin film investigated by L-edge X-ray absorption spectroscopy, J. Phys. Chem. C. 119 (2015) 4173–4179.

[36] S. Velu, K. Suzuki, S. Hashimoto, N. Satoh, F. Ohashi, S. Tomura, The effect of cobalt on the structural properties and reducibility of CuCoZnAl layered double hydroxides and their thermally derived mixed oxides, J. Mater. Chem. 11 (2001) 2049–2060.

[37] C. Maurizio, N. El Habra, G. Rossetto, M. Merlini, E. Cattaruzza, L. Pandolfo, M. Casarin, XAS and GIXRD study of Co sites in $CoAl_2O_4$ layers grown by MOCVD, Chem. Mat. 22 (2010) 1933–1942.

[38] S. Kurajica, J. Popović, E. Tkalček, B. Gržeta, V. Mandić, The effect of annealing temperature on the structure and optical properties of sol–gel derived nanocrystalline cobalt aluminate spinel, Mater. Chem. Phys. 135 (2012) 587–593.

[39] C.X. Kronawitter, J.R. Bakke, D.A. Wheeler, W. Wang, C. Chang, B.R. Antoun, J. Z. Zhang, J. Guo, S.F. Bent, S.S. Mao, L. Vayssieres, Electron enrichment in 3d transition metal oxide hetero-nanostructures, Nano Lett. 11 (2011) 3855–3861.

[40] M. Zhu, D. Guan, Z. Hu, H. Lin, C. Chen, H. Sheu, S. Wang, J. Zhou, W. Zhou, Z. Shao, Synergistic effects in ordered Co oxides for boosting catalytic activity in advanced oxidation processes, Appl. Catal. B: Environ. 297 (2021), 120463.

[41] X. Wu, J. Chen, M. Wang, X. Li, L. Yang, G. Li, L. Shan, X. Li, Y. Lin, J. Jiang, High-curvature carbon-supported Ni single atoms with charge polarization for highly efficient CO_2 reduction, Chem. Commun. 58 (2022) 2914–2917.

[42] Y. Yang, J. Jiang, X. Lu, J. Ma, Y. Liu, Production of sulfate radical and hydroxyl radical by reaction of ozone with peroxymonosulfate: A novel advanced oxidation process, Environ. Sci. Technol. 49 (2015) 7330–7339.

[43] J. Song, N. Hou, X. Liu, M. Antonietti, P. Zhang, R. Ding, L. Song, Y. Wang, Y. Mu, Asymmetrically coordinated CoB_1N_3 moieties for selective generation of high-valence Co-oxo species via coupled electron-proton transfer in Fenton-like reactions, Adv. Mater. 35 (2023), 2209552.

[44] X. Zhou, M. Luo, C. Xie, H. Wang, J. Wang, Z. Chen, J. Xiao, Z. Chen, Tunable S doping from Co_3O_4 to Co_9S_8 for peroxymonosulfate activation: Distinguished radical/nonradical species and generation pathways, Appl. Catal. B: Environ. 282 (2021), 119605.

[45] A. Jawad, K. Zhan, H. Wang, A. Shahzad, Z. Zeng, J. Wang, X. Zhou, H. Ullah, Z. Chen, Z. Chen, Tuning of persulfate activation from a free radical to a nonradical pathway through the incorporation of non-redox magnesium oxide, Environ. Sci. Technol. 54 (2020) 2476–2488.

[46] J.E. Yang, M. Zhu, X. Duan, S. Wang, B. Yuan, M. Fu, The mechanistic difference of ^1T–^2H MoS_2 homojunctions in persulfates activation: Structure-dependent oxidation pathways, Appl. Catal. B: Environ. 297 (2021), 120460.

[47] E. Yun, J.H. Lee, J. Kim, H. Park, J. Lee, Identifying the nonradical mechanism in the peroxymonosulfate activation process: Singlet oxygenation versus mediated electron transfer, Environ. Sci. Technol. 52 (2018) 7032–7042.

[48] Y. Zhou, J. Jiang, Y. Gao, J. Ma, S. Pang, J. Li, X. Lu, L. Yuan, Activation of peroxymonosulfate by benzoquinone: a novel nonradical oxidation process, Environ. Sci. Technol. 49 (2015) 12941–12950.

[49] Z. Yang, J. Qian, C. Shan, H. Li, Y. Yin, B. Pan, Toward selective oxidation of contaminants in aqueous systems, Environ. Sci. Technol. 55 (2021) 14494–14514.

[50] L. Lian, B. Yao, S. Hou, J. Fang, S. Yan, W. Song, Kinetic study of hydroxyl and sulfate radical-mediated oxidation of pharmaceuticals in wastewater effluents, Environ. Sci. Technol. 51 (2017) 2954–2962.

[51] R. Xiao, J. Ma, Z. Luo, W. Zeng, Z. Wei, R. Spinney, W.P. Hu, D.D. Dionysiou, Experimental and theoretical insight into hydroxyl and sulfate radicals-mediated degradation of carbamazepine, Environ. Pollut. 257 (2020) 113498.

[52] L. Lai, H. Ji, H. Zhang, R. Liu, C. Zhou, W. Liu, Z. Ao, N. Li, C. Liu, G. Yao, B. Lai, Activation of peroxydisulfate by V-Fe concentrate ore for enhanced degradation of carbamazepine: Surface $\equiv$V(III) and $\equiv$V(IV) as electron donors promoted the regeneration of $\equiv$Fe(II), Appl. Catal. B: Environ. 282 (2021), 119559.